Two-grating interferometer with sinusoidal phase modulation for surface profile measurement

Yande Xu
Osami Sasaki, MEMBER SPIE
Takamasa Suzuki, MEMBER SPIE
Niigata University
Graduate School of Science and Technology
8050 Ikarashi 2
Niigata, 950-2181 Japan

Abstract. A two-grating interferometer for measurement of profiles of polished surfaces is proposed. The ±first-order beams diffracted by the first grating produce parallel fringes of about 50-μm spacing on an object surface. By using the second grating, we eliminate the parallel fringes and extract a phase distribution produced by the surface profile of the object. Moreover, the vibration of the second grating of a small size enables us to use the sinusoidal phase-modulating interferometry. Measurement resolution is higher than 0.3 μm at the equivalent wavelength of 35 μm. © *2005 Society of Photo-Optical Instrumentation Engineers.*
[DOI: 10.1117/1.1883083]

Subject terms: surface profile measurement; grating interferometer; fringe projection; sinusoidal phase modulation.

Paper 040253 received May 6, 2004; revised manuscript received Aug. 31, 2004; accepted for publication Oct. 18, 2004; published online Mar. 31, 2005.

1 Introduction

Fringe projection and shadow moiré methods or grating interferometers are used to measure surface profiles with a large convex, concave, or step-shape object.[1-6] If a high measuring accuracy of a few microns is required, the period of the fringe pattern projected to the surface of an object must be a few hundred microns.[7-9] In this case, due to a limited resolution of a CCD image sensor, the fringe pattern should not have a large number of fringes. Thus, only small regions can be measured. In shadow moiré methods or grating interferometers, the fringe pattern projected on the surface is eliminated by using another grating and, thus, a wide measuring region can be obtained.[10-15] However, a large-size grating placed in front of the object must be displaced when using the phase shifting technique. An exact displacement of the large grating is not easy, and a high-speed displacement is impossible.

In this work, a two-grating interferometer is proposed in which a small size grating is vibrated sinusiodally for measuring profiles of polished surfaces with sinusoidally phase-modulating (SPM) interferometry.[16,17] The ±first-order beams diffracted by the first grating produce the parallel interference fringes on the object surface. By using the second grating, these two beams are diffracted in the direction of the optical axis, which enables us to eliminate the parallel fringes and extract a phase distribution produced by the surface profile of the object. Since the two interfering beams always have the same intensity, a good contrast pattern can be obtained. The small-size second grating is vibrated using SPM interferometry. An exact sinusoidal vibration can be easily given to the grating at a high frequency. This means that the two-grating interferometer proposed here can make surface profile measurements with high accuracy in a short period of time. A reduced-size image must be formed on the second grating. This image formation causes two limitations. One is the effect of lens aberration, which limits the size of the object. The other one is that the slope of the surface shape toward one direction is limited to a very small value. It is shown that in spite of these limitations, the interferometer proposed here is useful for measuring polished surfaces without a large slope along one direction.

2 Principle

Figure 1 shows a configuration of a two-grating interferometer using SPM interferometry for measuring a surface profile of a polished object. First, we explain roughly how to obtain a phase distribution corresponding to the surface profile from an interference pattern. The beam emitted from a laser diode (LD) is collimated with a lens L_0 and is incident to a binary step grating G_1. This collimated beam is diffracted by the grating G_1 into multiple-grade parallel beams with different directions of propagation, and is projected onto an object surface. In these beams, the +first- and −first-order beams produce the interference fringes of spacing $P_1/2$, as shown in Fig. 2. The two-pinhole diaphragm H_1 placed on the common focal plane of lenses L_1 and L_2 passes the optical waves, which are produced from the +first- and −first-order beams through reflection by the object surface. An afocal imaging system with lens L_1 and L_2 forms an image of the object surface on grating G_2. The diaphragm H_2 placed on the common focal plane of lenses L_3 and L_4 selects the optical waves beams that are diffracted by grating G_2 in the directions almost identical to the optical axis. These two beams make an image of the object surface on the CCD image sensor with an afocal imaging system with lenses L_3 and L_4. There is no parallel interference fringes of period $P_1/2$ in this image. The phase distribution of the interference pattern on the CCD image sensor is caused by only the surface profile of the object.

Next, some equations of the optical fields in the interferometer are derived under the assumption that only the +first- and −first-order beams are projected onto the ob-

0091-3286/2005/$22.00 © 2005 SPIE

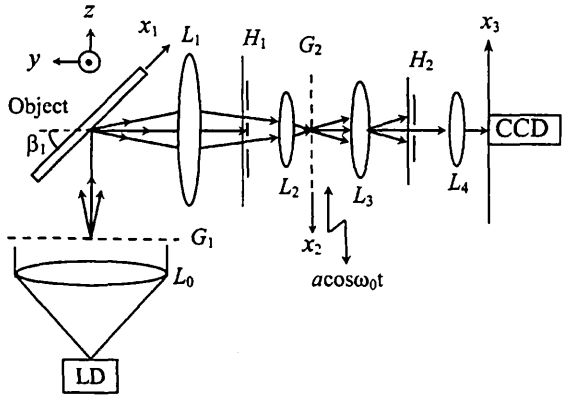

Fig. 1 Two-grating interferometer using sinusoidal phase-modulating interferometry.

ject. The intensity distribution produced by the +first- and −first-order beams is expressed as

$$I(x,y_1)=1+\cos(4\pi x/P_1). \tag{1}$$

Equation (1) shows that the interference fringes of $P_1/2$ spacing in the x direction are parallel to the y-z plane as shown in Fig. 2. A surface profile of the object is expressed by $r(x_{1R},y_1)$, which is normal to a reference plane intersecting with the x axis at an angle of β_1. The intensity distribution produced on the object surface is imaged onto the second grating G_2 by a focal imaging system with lenses L_1 and L_2, whose focal lengths are f_1 and f_2, respectively. The magnification of the image system is given by $M_{21}=f_2/f_1$. The reflection by the polished object rotates the x-z plane by $2\beta_1$, and the intersection angle between the optical axis of the imaging system and the reference plane is $(\pi/2)-\beta_1$. The imaging system regards the surface profile of $r(x_{1R},y_1)$ to be positioned on the coordinate of (x_1,y_1) and have a length of $r(x_{1R},y_1)/\cos\beta_1$ along the optical axis, as shown in Fig. 2. Expressing this surface profile detected with the imaging system as $r_D(x_1,y_1)=r(x_{1R},y_1)/\cos\beta_1$, the intensity distribution on the object surface is given by

$$I(x_1,y_1)=1+\cos\left[\frac{4\pi(\cos\beta_1)x_1}{P_1}+\frac{4\pi r_D(x_1,y_1)\sin 2\beta_1}{P_1}\right]. \tag{2}$$

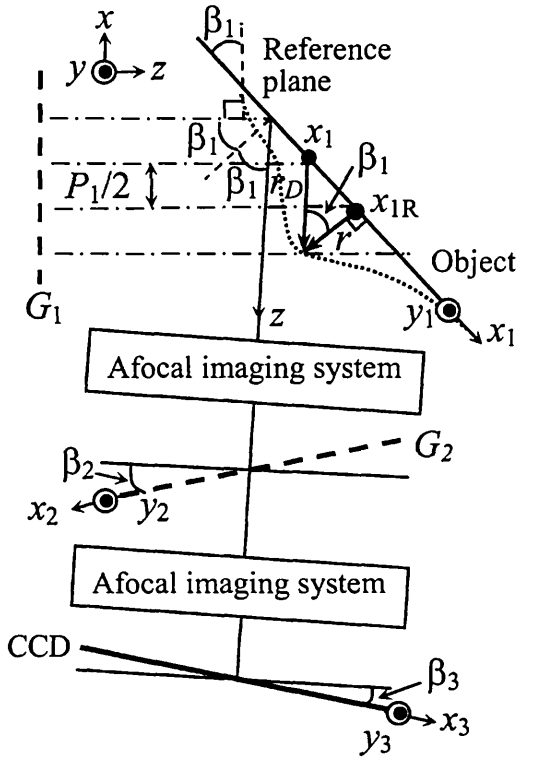

Fig. 2 Afocal imaging systems for the interference fringe pattern on an object.

The second grating G_2 must be inclined from the focal plane of lens 2 by an angle of β_2, which is given by

$$\tan\beta_2=M_{21}\tan\beta_1. \tag{3}$$

Denoting the coordinate on the grating G_2 by (x_2,y_2), the relations between the coordinates (x_1,y_1) and (x_2,y_2) are given by

$$x_1=\frac{\cos\beta_2}{M_{21}\cos\beta_1}x_2,\quad y_1=\frac{1}{M_{21}}y_2. \tag{4}$$

Substituting Eq. (4) into Eq. (2), the intensity distribution produced on the second grating G_2 is written as

$$I(x_2,y_2)=1+\cos\left(\frac{4\pi x_2}{P_1M_G}+\alpha\right), \tag{5}$$

where

$$M_G=\frac{M_{21}}{\cos\beta_2}\quad\text{and}\quad\alpha=\frac{4\pi r_D(x_1,y_1)\sin 2\beta_1}{P_1}.$$

The complex amplitudes of the two fields on grating G_2 are expressed as

$$U_{\pm 1}(x_2)=(1/\sqrt{2})\exp(\pm i2\pi x_2/P_1M_G)\exp(\pm i\alpha/2). \tag{6}$$

The binary grating G_2 is vibrating along the x_2 axis with the form of $a\cos\omega_0 t$ to adopt the sinusoidal phase-modulating interferometry. In this case, the required diffraction effects of the grating G_2 are expressed as

$$\exp[\pm i2\pi(x_2-a\cos\omega_0 t)/P_2]. \tag{7}$$

When the condition of $1/P_1M_G=1/P_2$ is satisfied, the diffraction effects given by Eq. (7) convert the fields given by Eq. (6) to the following fields, respectively,

$$U_{+1,-1}(x_2,y_2)=(1/\sqrt{2})\exp[i(z/2)\cos\omega_0 t+i(\alpha/2)], \tag{8}$$

$$U_{-1,+1}(x_2,y_2)=(1/\sqrt{2})\exp[-i(z/2)\cos\omega_0 t-i(\alpha/2)], \tag{9}$$

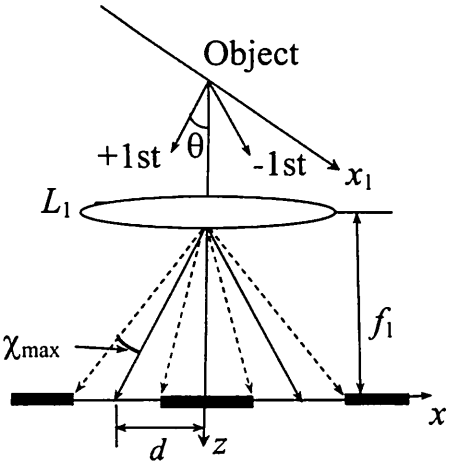

Fig. 3 Relations between the reflected lights and the slits on diaphragm H_1.

where $z=4\pi a/P_2$. These fields are selected with the diaphragm H_2 in the afocal imaging system with lenses L_3 and L_4, whose focal lengths are f_3 and f_4, respectively. The magnification of the image system is given by $M_{32}=f_4/f_3$. The surface of the CCD image sensor must be inclined from the focal plane of lens 4 by an angle of β_3, which is given by

$$\tan\beta_3=M_{32}\tan\beta_2. \tag{10}$$

Denoting the coordinate on the surface of the CCD image sensor by (x_3,y_3), the relations between the coordinates (x_2,y_2) and (x_3y_3) are given by

$$x_2=\frac{\cos\beta_3}{M_{32}\cos\beta_2}x_3, \quad y_2=\frac{1}{M_{32}}y_3. \tag{11}$$

With the expressions of $x_3=x_1/M_{CG}$ and $y_3=y_1/M_{31}$, Eqs. (4) and (11) provide

$$M_{31}=M_{32}M_{21}, \quad M_{CG}=\frac{M_{31}\cos\beta_1}{\cos\beta_3}. \tag{12}$$

The intensity distribution produced on the CCD image sensor is given by

$$I(t,x_3,y_3)=1+\cos[z\cos\omega_0 t+\alpha]. \tag{13}$$

The phase α on the detecting point of (x_3,y_3) is extracted from the time-varying detected intensity or the sinusoidally phase-modulated interference signal given by Eq. (13) with the sinusoidal phase-modulating interferometry.[16,17] Using the relation of $x_{1R}=x_1+r_D\sin\beta_1$, the following surface profile is obtained from the phase α:

$$r(x_{1R},y_1)=r_D(x_1,y_1)\cos\beta_1=\frac{P_1}{8\pi\sin\beta_1}\alpha. \tag{14}$$

Finally, it is explained how the configuration of the interferometer shown in Fig. 1 brings some limitations on what kind of object surface can be measured. After the ±first-order beams are reflected by the surface object, the reflected lights pass through the rectangular slit of diaphragm H_1, as shown in Fig. 3. The intersection angle between the two beams and the optical axis z is $\theta\simeq\lambda/P_1$, where λ is the wavelength of the LD. The centers of the two rectangular slits along the x axis are separated from the optical axis z by a distance of $d\simeq f_1\lambda/P_1$ in the opposite directions, respectively, and the width of the slits along the x axis is d. In this situation, the maximum propagation angle of the reflected waves is limited to $\chi_{max}=\theta/2$, which follows the limitation on the slope of the surface shape along the x_1 axis as follows:

$$\frac{\partial r(x_1,y_1)}{\partial x_1}=\tan(\phi_x)<\tan(\theta/4). \tag{15}$$

Since there is a strong limit on the slope of the surface shape along the y_1 axis, surface profiles without a large slope along the x_1 axis can be measured well. The other limitation is on the size of the object, which is caused by the aberrations of the lenses in the imaging systems. Effects of the aberrations are shown experimentally in the next section.

3 Experiments

The two-grating interferometer shown in Fig. 1 was constructed. The parameters used in the interferometer were as follows: $P_1=99.5\,\mu$m, $\beta_1=45$ deg, $f_1=300$ mm, $f_2=30$ mm, $M_{21}=1/10$, $\beta_2=5.7$ deg, $M_G=1/9.95$, $P_2=P_1M_G=10.0\,\mu$m, $f_3=100$ mm, $f_4=20$ mm, $M_{32}=1/5$, $\beta_3=1.1$ deg, and $\lambda=0.66\,\mu$m. The diameters of lenses 1 and 2 were $D_1=100$ mm and $D_2=30$ mm, respectively. The sizes of gratings G_1 and G_2 were 100×100 mm^2 and 10×10 mm^2, respectively. The grating G_2 was vibrating with $\omega_0/2\pi=62.5$ Hz. A high-speed CCD image sensor was used to detect the sinusoidally phase-modulated interference signal. The frame rate of the CCD image sensor was $8\times(\omega_0/2\pi)$. The length of the detected interference signal was $4\times(2\pi/\omega_0)=0.064$ s.

First, the effect of the lens aberration was examined, which limits the size of the object to be measured. Since the space of P_2 was fixed, the space of P_1 was adjusted by rotating the grating G_1 of 100-μm spacing so that no parallel fringe pattern appeared on the CCD image sensor when the object was a plane mirror. A fringe pattern on the image of an 80-mm-diam mirror was observed as shown in Fig. 4. This fringe pattern was caused mainly by the aberration of lens 2. The phase distribution $\alpha(x_3,y_3)$ of the fringe pattern of Fig. 4 was measured by detecting the interference signal. A region of about 30×30 mm^2 was used as the measuring region, where the distribution of the phase α had a small fluctuation less than $2\pi/100$. The phase α changed by 2π when the surface profile $r(x_{1R},y_1)$ changed by $P_1/2\sqrt{2}=35.3\,\mu$m. This value of 35.3 μm is referred to as an equivalent wavelength in the two-grating interferometer.

Second, a profile of a polished metal surface was employed as an object. The object had a 1-D concave surface

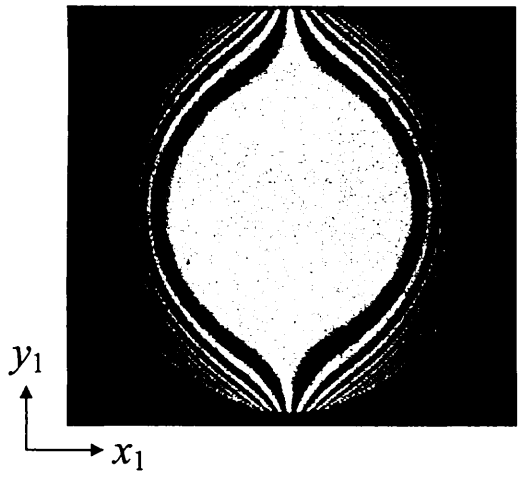

Fig. 4 Detected interference pattern involving the aberrations of a lens.

with about 20 μm depth in the center region along the y_1 axis. Since the depth of the concave surface was less than the equivalent wavelength of 35.3 μm, a small number of the measurement points could detect the phase distribution on the surface in the region of 30×30 mm^2. A smaller number of the measurement points provided a higher speed measurement. Thus the number of the measurement points was selected to be 80×80. The pixel size of the CCD image sensor was 7.4 μm, and the intervals of the measurement points along the x and y axes on the object surface were 0.53 and 0.37 mm, because of $M_{CG}=0.014$ and $M_{31}=0.02$, respectively. The time-varying interference pattern of the surface profile or the sinusoidal phase-modulated interference signals were detected in the x_3-y_3 plane with the CCD image sensor, and the phase distribution $\alpha(x_3,y_3)$ of the interference signals was calculated with sinusoidal phase-modulating interferometry. Since the coordinate (x_3,y_3) corresponded to the coordinate (x_1,y_1), the value of $r_D(x_1,y_1)$ was obtained directly from the phase distribution. To obtain the distribution of $r(x_{1R},y_1)$ from the distribution of $r_D(x_1,y_1)$, the coordinate of x_1 must be calculated with the relation of $x_{1R}=x_1+r_D\cos\beta_1$. Since the values of $r_D(x_1,y_1)$ were less than 20 μm, the differences between the measured distributions of $r_D(x_1,y_1)$ and $r(x_{1R},y_1)$ were less than 0.3 μm. From this result, it could be assumed that the coordinate of x_1 was equal to that of x_{1R}. Figure 5 shows a measured surface profile of $r(x_{1R},y_1)$, where the coordinates (x,y) are used instead of (x_{1R},y_1). The surface profiles along the two lines of $x=15$ mm and $y=15$ mm are shown in Figs. 6(a) and 6(b),

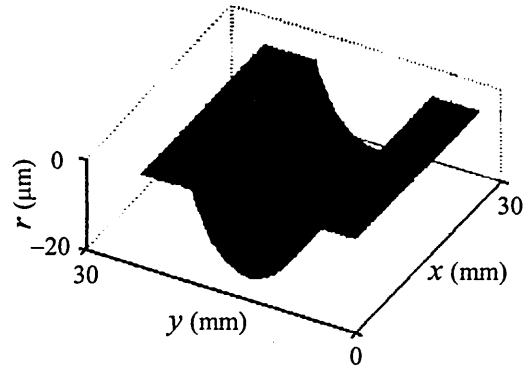

Fig. 5 Measured profile of the polished metal surface in the x-y plane.

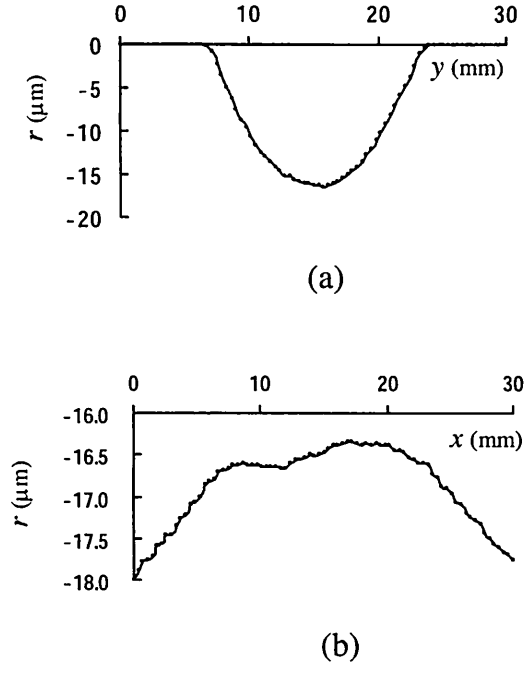

Fig. 6 Surface profile measured with the interferometer on the two lines of (a) $x=15$ mm and (b) $y=15$ mm.

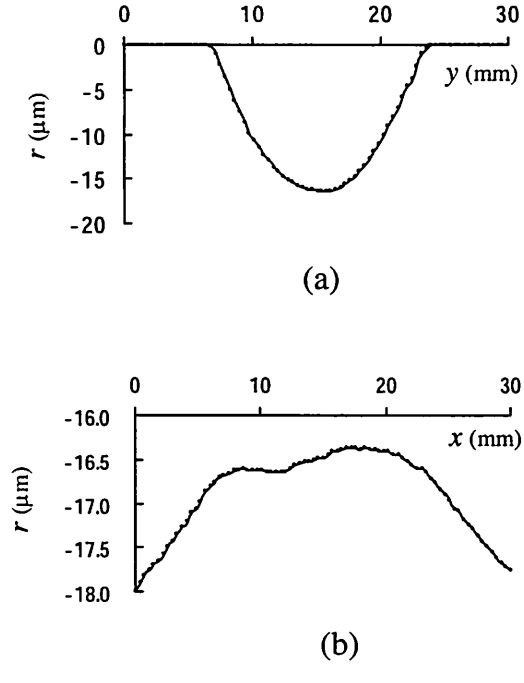

Fig. 7 Surface profile measured with a Taylor Hobson instrument on the two lines of (a) $x=15$ mm and (b) $y=15$ mm.

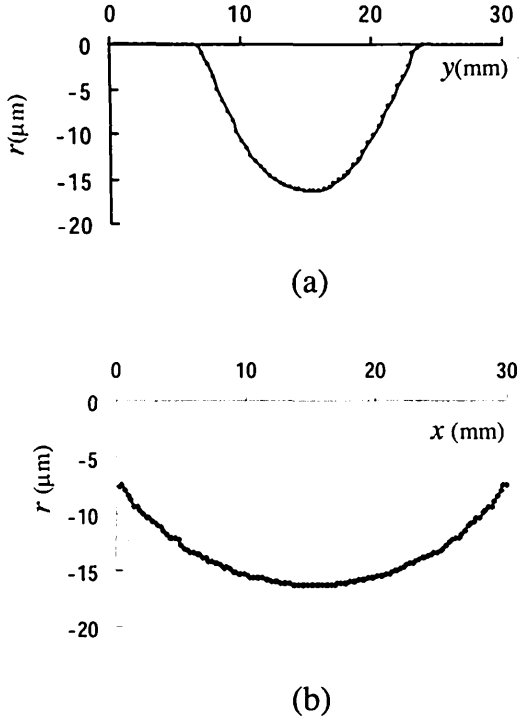

Fig. 8 Surface profile measured at the rotation angle γ of 10 deg on the two lines of (a) $x=15$ mm and (b) $y=15$ mm.

respectively. The measurements of the same object were repeated at intervals of a few minutes. The difference between the two measured results was less than ~0.3 μm in rms value. The surface profile was also measured with a Taylor Hobson instrument, whose measurement resolution was 0.2 μm, as shown in Figs. 7(a) and 7(b). The surface profile measured with the interferometer proposed here was almost the same as that measured with the contact-type instrument. Figures 6(a) and 6(b) indicate that the measurement points of 80×80 were sufficient to represent the surface profiles of simple concave shapes.

Third, the effects of the limitation on the reflected angle shown in Fig. 3 were examined. From Eq. (15), the slope of the surface profile along the x axis had to be less than 1.6×10^{-3} rad. Since the slope along the x axis was a very small value in the measurements shown in Figs. 5 and 6, good results were obtained. The object was rotated in the x-y plane toward the x axis by an angle of γ. The surface

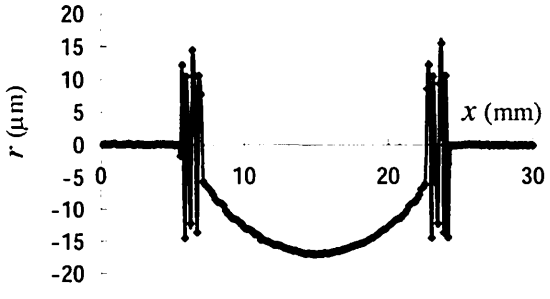

Fig. 9 Surface profile measured at the rotation angle γ of 12 deg on the line of $y=15$ mm.

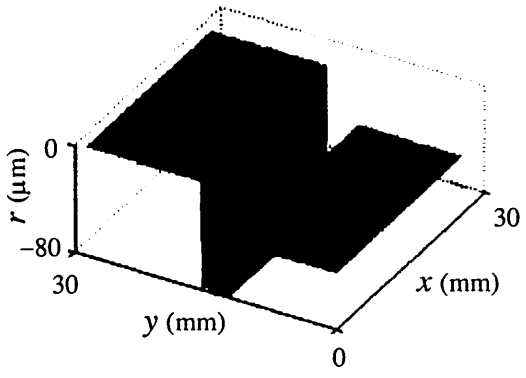

Fig. 10 Measured profile of the polished step surface in the x-y plane.

profile could be measured at $\gamma=10$ deg, as shown in Figs. 8(a) and 8(b) on the two lines of $x=15$ mm and $y=15$ mm, respectively. The slope φ of the surface profile along the x axis at $y=15$ mm was less than 1.6×10^{-3}. Almost every reflected light from the object surface passed through the slits of the diagram H_1. When the rotation angle γ was 12 deg, all of the reflected lights could not pass through the slits. Figure 9 shows the measured surface profile along the x axis on the line of $y=15$ mm. Since the slope of the surface profile along the x axis exceeded 1.6×10^{-3}, the surface profile could not be measured.

Finally, another polished surface with a step shape was measured. The object had a deep groove with about 2.5 mm width between the two planar surfaces. No light was reflected from the groove region. Figure 10 shows the measured profile of the step surface in the x-y plane. The measured surface profile on $x=15$ mm is shown in Fig. 11. Since it was known beforehand that the step width was around 30 μm, the measured step width was regarded to be larger than the equivalent wavelength of 35 μm. The measurements of the same object were repeated at intervals of a few minutes, and the difference between the two measured results was also less than ~0.3 μm in rms value. The measured surface profile of Fig. 11 agreed with that measured with the Taylor Hobson instrument.

4 Conclusion

In this work, a two-grating interferometer using SPM interferometry for measuring polished surface profiles is proposed. The characteristics on the optical imaging system of the interferometer are also analyzed. It is made clear what

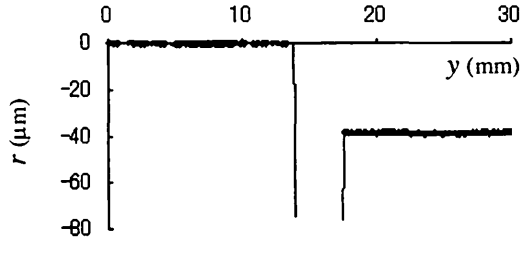

Fig. 11 Measured profile of the step surface on the line of $x=15$ mm.

quantity of the surface profile is detected from the interference fringe on the CCD image sensor. By using the second grating G_2, the parallel fringes are eliminated and a phase distribution produced by the surface profile of the object is extracted. Measurement resolution is higher than 0.3 μm at the equivalent wavelength of 35 μm. Although the image system requires the small size of the object and the small slope in the surface shape along one direction, it is shown that the interferometer proposed here is useful for measuring polished surfaces without a large slope along one direction.

References

1. K. Creath and J. C. Wyant, "Moiré and fringe projection techniques," in *Optical Shop Testing*, D. Malacara, Ed., pp. 653–685, Wiley, New York (1992).
2. S. H. Rowe and W. T. Welford, "Surface topography of non-optical surfaces by projected interference fringes," *Nature (London)* **216**, 786–787 (1967).
3. G. Indebetouw, "Profile measurement using projection of running fringes," *Appl. Opt.* **17**, 2930–2933 (1978).
4. M. Takeda and K. Mutoh, "Fourier transform profilometry for the automatic measurement of 3-d object shapes," *Appl. Opt.* **22**, 3977–3982 (1983).
5. V. Srinivasan, H. C. Liu, and M. Halioua, "Automated phase-measuring profilometry of 3-D diffuse objects," *Appl. Opt.* **23**, 3105–3108 (1984).
6. J. Villa, M. Servin, and L. Castillo, "Profilometry for the measurement of 3-D object shapes based on regularized filters," *Opt. Commun.* **161**, 13–18 (1999).
7. R. Windecker and H. J. Tiziani, "Topometry of technical and biological objects by fringe projection," *Appl. Opt.* **34**, 3644–3650 (1995).
8. R. Windecker, S. Franz, and H. J. Tiziani, "Optical roughness measurements with fringe projection," *Appl. Opt.* **38**, 2837–2842 (1999).
9. T. Tkaczyk and R. Józwicki, "Influence of optical imaging on phase measurements in fringe projection coherent systems," *Opt. Eng.* **41(4)**, 811–821 (2002).
10. D. M. Meadows, W. O. Johnson, and J. B. Allen, "Generation of surface contours by moiré patterns," *Appl. Opt.* **9**, 942–947 (1970).
11. H. Takasaki, "Moiré topography," *Appl. Opt.* **9**, 1467–1472 (1970).
12. H. Takasaki, "Moiré topography," *Appl. Opt.* **12**, 845–850 (1973).
13. P. de Groot, "Grating interferometer for flatness testing," *Opt. Lett.* **21**, 228–230 (1996).
14. P. de Groot, X. C. de Lega, and D. Stephenson, "Geometrically desensitized interferometry for shape measurement of flat surfaces," *Opt. Eng.* **39(1)**, 86–90 (2000).
15. P. de Groot, "Diffractive grazing-incidence interferometer," *Appl. Opt.* **39**, 1527–1530 (2000).
16. O. Sasaki and H. Okazaki, "Detection of time-varying intensity distribution with CCD image sensors," *Appl. Opt.* **24**, 2124–2126 (1985).
17. O. Sasaki and H. Okazaki, "Sinusoidal phase modulating interferometry for surface profile measurement," *Appl. Opt.* **25**, 3137–3140 (1986).

Biographies and photographs of authors not available.